JES Focus Issue on Mathematical Modeling of Electrochemical Systems at Multiple Scales in Honor of John Newman

Two-Dimensional Computational Fluid Dynamics Analysis of Transport Limitations of Different Electrolyte Systems in a Lithium-Air Button Cell Cathode

Manik Mayur[z] and Wolfgang G. Bessler[*]

Institute of Energy Systems Technology (INES), Offenburg University of Applied Sciences, 77652 Offenburg, Germany

One of the practical bottlenecks associated with commercialization of lithium-air cells is the choice of an appropriate electrolyte that provides the required combination of cell performance, cyclability and safety. With the help of a two-dimensional multiphysics model, we attempt to narrow down the electrolyte choice by providing insights into the effect of the transport properties of electrolyte, electrode saturation (flooded versus gas diffusion), and electrode thickness on a single discharge performance of a lithium-air button cell cathode for five different electrolytes including water, ionic liquid, carbonate, ether, and sulfoxide. The 2D distribution of local current density and concentrations of electrochemically active species (O_2 and Li^+) in the cathode is also discussed w.r.t electrode saturation. Furthermore, the efficacy of species transport in the cathode is quantified by introducing two parameters, firstly, a transport efficiency that gives local insight into the distribution of mass transfer losses, and secondly, an active electrode volume that gives global insight into the cathode volume utilization at different current densities. A detailed discussion is presented toward understanding the design-induced performance limitations in a Li-air button cell prototype.

Manuscript submitted April 3, 2017; revised manuscript received June 2, 2017. Published June 23, 2017. *This paper is part of the JES Focus Issue on Mathematical Modeling of Electrochemical Systems at Multiple Scales in Honor of John Newman.*

Lithium-air (Li-air) batteries are a promising alternative to the currently popular Li-ion batteries due to their significantly higher theoretical energy densities. Recently, considerable effort has been made in optimizing the cell performance and durability of Li-air battery cells either by modifying cell chemistry with the help of solvents,[1–5] salts[6–11] and redox mediators,[12–19] or by improving mechanistic and electrochemical properties of electrodes via an appropriate choice of support structure[20] and catalyst.[21,22] Given the multitude of choices for solvent and salt combinations in the literature, Balaish et al.[23] performed an extensive review of physio-chemical properties of the state-of-art electrolytes and combinations thereof, to assess performance of Li-air batteries. Depending upon the electrochemistry and solubility of the discharge products, the performance of Li-air cells can be severely affected, either due to salt deposition related electrode surface passivation[24–27] or pore clogging.[28,29] However, it has been demonstrated that with improved cell chemistry and electrode materials, such problems can be mitigated.[7]

An efficient cell design in combination with appropriate electrolyte choice is also an important aspect of improving cell performance. The sensitivity of cell performance to electrolyte properties and cell design has been extensively studied in the literature. Xu et al.[30] studied the effect of salt concentrations in non-aqueous electrolytes and compositions of solvent mixtures on a Li-air cell performance and concluded that lithium bis(trifluoromethanesulfonylimide) (LiTFSI) is the best-performing salt for a propylene carbonate (PC)-ethylene carbonate (EC) solvent mixture. Zheng et al.[31] proposed a dual electrolyte system wherein an aqueous electrolyte was used at cathode and an organic electrolyte was used at anode. They found that the major performance limitation in such batteries arises due to low solubility of O_2 in aqueous electrolytes in cathode. Wang and Cho[32] performed a 2D modeling of a Li-O_2 cell and demonstrated that at higher current densities, O_2 starvation occurs in large parts of cathode away from the O_2 inlet that reduces the O_2 reduction reaction (ORR) rates and adversely affects the cell performance. They highlighted the need of geometrical optimization of cathode structure to avoid O_2 starvation related losses. Tan et al.[33] proposed a cathode with stepwise porosity gradient to enhance O_2 penetration. Xia et al.[34] studied the effect of electrolyte volume in porous cathode on the cell performance. They found that the partially wetted cathodes have higher rate capability and specific capacity than a flooded cathode. The enhanced cell performance is due to faster penetration of O_2 in the cathode pores. Williford et al.[35] proposed to enhance the cell performance by using a dual-pore electrode and a "time-release" method of activating catalysts.

Although, Li-O_2 cell seems an exciting alternative to the Li-ion cell, it requires a dedicated supply of O_2 that might enhance the complexity and maintenance of the system, specifically in mobile applications. Geng et al.[36] reviewed the challenges of a Li-air system by providing interesting guidelines for replacing a Li-O_2 system with a Li-air system. One of the major challenges for a Li-air system is the lower partial pressure of O_2 that might significantly reduce the cell performance. Some efforts have been made to enhance the Li-air cell performance by either exploring the cathode materials[37] or even by designing fuel cell inspired flow fields.[38]

Most of the above investigations are experimental in nature that provide useful insights into global cell performance as a function of various cell operating conditions. However, it is always advantageous to understand the underlying physical processes responsible for the observed effect of parameter variation on local as well as global cell performance. Modeling and simulation studies are useful to analyze local transport processes and help to pin-point bottlenecks in achieving the theoretical Li-air cell performance.[39] With the help of modeling studies and experimentally obtained electrolyte data, a considerable amount of time and resources can be saved to anticipate the performance limiting or enhancing physio-chemical parameters and phenomena, and material cost. Hence, in order to create a high-performance battery, a multiscale investigation of simultaneous effects of local electrochemistry, species transport and cell component design has to be performed. One of the objectives of the current work is to study capacity-limitation in Li-air cells due to "under-utilization" of cathode pore volume because of reactant transport losses. A non-uniform supply of active species to the electrode/catalyst surface[40,41] leads to heterogeneity in electrode utilization. Such a situation arises due to a slow, diffusion-limited reactant supply at porous electrodes, especially during higher discharge currents. Moreover, reactant transport is not only affected by cell operating conditions like pressure and temperature, but also by the composition and concentration of electrolytic salts and other additives like redox mediators. Consequently,

*Electrochemical Society Member.
[z]E-mail: manik.mayur@hs-offenburg.de

in order to create an efficient and high-performance Li-air cell, a significant focus on cell design and cell geometry is also required.

We present a modeling and simulation analysis of a Li-air button cell focusing on the effect of various electrolyte properties and cell geometric parameters on cell performance and cathode utilization. Electrolytes from various solvent classes are systematically compared – namely aqueous, ionic liquids, organic carbonates, organosulfur, and protic ethers. Here, the electrolyte comparison is limited to the cell performance based on transport parameters of electrochemically active species in the electrolyte. However, it has to be noted that other challenges for the choice of a battery electrolyte exist, such as, electrochemical stability window, thermal stability, vapor pressure, toxicity, side reactions with reaction intermediates, etc.[42] Hence, complementary to this study, further investigations must be made on the above physio-chemical properties for a practical choice of the electrolyte. Further, we also analyze the influence of cathode thickness and electrolyte saturation in the porous cathode on cell performance with the help of appropriate characteristic figures. The modeled Li-air cell is assumed to be open to the ambient atmosphere. With a 2D multiphysics simulation of axi-symmetric cell geometry, it is demonstrated that with appropriate and harmonized choice of electrolyte and air transport strategy a cell performance can be tuned to the desired performance.

Modeling and Simulation

In the present work the major focus is on mass and charge transfer effects in the cathode half-cell of a Li-air button cell, as slow O_2 and Li^+ transport in the cathode is one of the leading cause for the cell performance loss. Transport processes and electrochemistry in the separator and anode are assumed fast (not rate co-limiting). The anode acts as a line source of Li^+ based on a modified Butler-Volmer equation. The cathode electrochemistry is also represented by a modified Butler-Volmer equation. Since, O_2 transport in the porous cathode strongly depends on the choice of the electrolyte, five different types of electrolytes are compared. Furthermore, we explore two different electrode-electrolyte configurations, that is, flooded electrode and gas diffusion electrode. The entire modelling approach and the governing equations are discussed in detail in the following sections.

Simulation geometry.—Figure 1 shows the modeling domain in which the button cell is modeled as a 2D axisymmetric geometry. The cell's main structural elements consist of an air inlet hole in the cell cover at the top, a porous gas diffusion layer (GDL) that distributes air onto the cathode surface, and the porous cathode. As this study focuses on transport processes in the cathode only, the separator and lithium anode are not explicitly a part of the modeling domain, but are represented through boundary conditions. Table I lists the cell dimensions used in the current study.

Basic model assumptions.—The present analysis is limited to a cell discharge process where the major discharge product of the ORR, viz., hydroxide ion (OH^-) in aqueous solvent and peroxide ion (O_2^{2-}) in the organic solvents, are assumed to have no influence on the transport of the dissolved O_2 and Li^+ in the electrolyte. Therefore, effects like electrode surface passivation or porosity reduction that can significantly affect cell performance are not captured. Also, there

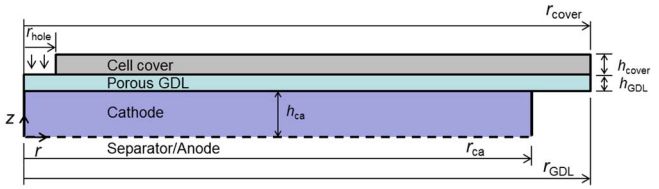

Figure 1. 2D axi-symmetric modeling domain that represents the button cell geometry with air inlet hole marked by arrows.

Table I. Geometrical parameters of the 2D axi-symmetric cell model.

Cell component	Radius/mm	Thickness/mm
Cell cover	$r_{cover} = 25$	$h_{cover} = 0.3$
Inlet hole	$r_{hole} = 1$	$h_{hole} = 0.3$
Porous GDL	$r_{GDL} = 25$	$h_{GDL} = 0.235$
Cathode	$r_{ca} = 20$	$h_{ca} = 0.235$

is lack of conclusive reaction mechanisms for the discharge products and their solubility data for all different classes of electrolytes considered. Complementary to the present approach, we have previously investigated detailed-chemistry 1D models that include the full multi-step chemistry/precipitation/phase-change mechanisms for aqueous and ether-based electrolytes.[19,43,44] The investigated current/voltage behavior thus represents an early stage of cell discharge. A low solubility of nitrogen and water vapor in the electrolytes is assumed so that explicit transport equations are not required for them. Thus, the species transport within the electrolyte is confined to the transport of O_2 and Li^+. The gas and the electrolyte phases are considered to be ideal, incompressible and isothermal. Consequently, the transport parameters for a given electrolyte are taken as constant. Further, the ionic species transport is modeled via dilute solution theory. For the purpose of this work, the species transport parameters needed for concentrated solution theory for different electrolytes were not available in the existing literature.

Transport in porous GDL.—The porous GDL contributes to the distribution and supply of air from the inlet hole of the button cell on to the cathode surface. Hence, it is modeled by classical gas transport equations for a porous medium, where the mass conservation equation can be written as,

$$\frac{\partial\left(\varepsilon_{GDL}\rho_{air,GDL}\right)}{\partial t} + \nabla\cdot\left(\rho_{air,GDL}\boldsymbol{u}_{air,GDL}\right) = 0 \qquad [1]$$

where, ε_{GDL} is the porosity of the GDL and $\rho_{air,GDL}$ is the density of air in the GDL. Here, air is assumed to be an ideal gas consisting of N_2, O_2, and water vapor, where its density is related to the pressure as, $\rho_{air,GDL} = \frac{\sum_i c_{i,GDL} M_i}{\sum_i c_{i,GDL}} \frac{p_{air,GDL}}{RT}$. Here, $c_{i,GDL}$ is the molar concentration and M_i is the molar mass of the constituent species, R is the ideal gas constant, and $T = 298.15$ K is the cell temperature. The flow velocity in the porous GDL is calculated by Darcy's law as,

$$\boldsymbol{u}_{air,GDL} = -\frac{\kappa_{air,GDL}}{\mu_{air,GDL}}\nabla p_{air,GDL} \qquad [2]$$

where, $\kappa_{air,GDL}$ is permeability and $\mu_{air,GDL}$ is viscosity of air respectively. The species conservation equation in the gas phase within GDL is written as,

$$\frac{\partial\left(\varepsilon_{GDL}c_{i,GDL}\right)}{\partial t} - \nabla\cdot\left(D_i^{eff}\nabla c_{i,GDL}\right) + \nabla\cdot\left(c_{i,GDL}u_{air,GDL}\right) = 0. \qquad [3]$$

The effective diffusion coefficient, D_i^{eff} is related to the species diffusion coefficient (D_i) according to the Bruggeman correction as $D_i^{eff} = \varepsilon_{GDL}^{1.5} D_i$. Here, the choice of Fick's diffusion over Maxwell-Stefan multi-component diffusion formulation was motivated by the work of Lindstrom et al.[45] They demonstrated that for humidified ambient air in porous media, Fick's diffusion has comparable results than that of Maxwell-Stefan diffusion. Further, using Fick's diffusion reduced the computational complexity of the governing equations, enabling us to use finer meshing at the inlet and outlet boundaries where high concentration gradients were expected.

At the inlet, air is assumed to have a low relative humidity of $R_H = 10\ \%$ at standard temperature and pressure (STP). The inlet partial pressure of water vapor is calculated as,

$$p_{H_2O,in} = R_H \cdot p^{sat} \qquad [4]$$

where, the saturation pressure of water vapor (p_{sat}) in Pascal is calculated as a function of temperature (in °C) as,[46]

$$\log_{10} p^{sat} = 5.9464 - \frac{1730.63}{(233.426 + T)}. \quad [5]$$

The partial pressure of O_2 is calculated as, $p_{O_2,in} = 0.21(1 - \frac{p_{H_2O,in}}{p_{atm}})$ and that of nitrogen is calculated as, $p_{N_2,in} = p_{atm} - p_{H_2O,in} - p_{O_2,in}$. The inlet species concentrations are then calculated as,

$$c_{i,in} = \frac{p_{i,in}}{RT}. \quad [6]$$

Electrochemistry model.—In this work, a generic one-step ORR is considered in cathode, which is represented by,

$$Li^+_{el} + \frac{1}{n}O_2 + e^- \rightarrow \text{Products} \quad [7]$$

where, n is 2 for organic solvents and 4 for aqueous solvent.[44,47] The above mentioned charge-transfer reaction is represented by a modified Butler-Volmer equation that relates the cathodic volumetric current density ($i^{\mathbb{V}}_{ca}$) to the cathode activation overpotential (η^{act}_{ca}) as,

$$i^{\mathbb{V}}_{ca} = Fk^0_{ca}A^{\mathbb{V}}\left(\frac{c_{O_2,el}}{c^{ref}}\right)^{(1-\alpha)/n}\left(\frac{c_{Li^+,el}}{c^{ref}}\right)^{1-\alpha} \times \left\{e^{\alpha F\eta^{act}_{ca}/(RT)} - e^{-(1-\alpha)F\eta^{act}_{ca}/(RT)}\right\} \quad [8]$$

where, $k^0_{ca} = 1 \times 10^{-15}$ mol/(m^2 · s) is the assumed rate[26] of the ORR, $A^{\mathbb{V}} = 10^6$ m^2/m^3 is the volume specific electrode area, $c_{O_2,el}$ is the local concentration of dissolved O_2 in the electrolyte, $c^{ref} = 1$ M is the reference concentration, $F = 96485$ C/mol is the Faraday constant, $\alpha = 0.5$ is the symmetry factor, and η^{act}_{ca} is calculated as,[48,49]

$$\eta^{act}_{ca}(r, z) = \Delta\phi_{ca}(r, z) - \Delta\phi^{eq}_{ca}(r, z) \quad [9]$$

where, $\Delta\phi_{ca} = \phi_{ca} - \phi_{el}$ is the local Galvani potential difference between the electrode (ϕ_{ca}) and electrolyte (ϕ_{el}) in the cathode, and $\Delta\phi^{eq}_{ca}$ is the equilibrium Galvani potential difference given by the Nernst equation,

$$\Delta\phi^{eq}_{ca} = \Delta\phi^0_{ca} + \frac{RT}{F}\ln\left(\left(\frac{c_{O_2,el}}{c^0_{O_2,el}}\right)^{\frac{1}{n}}\left(\frac{c_{Li^+,el}}{c^0_{Li^+,el}}\right)\right) = \phi^0_{ca} - \phi^0_{el} + \frac{RT}{F}\ln\left(\left(\frac{c_{O_2,el}}{c^0_{O_2,el}}\right)^{\frac{1}{n}}\left(\frac{c_{Li^+,el}}{c^0_{Li^+,el}}\right)\right) \quad [10]$$

where, ϕ^0_{ca} is the standard cathode potential in unpolarized state, ϕ^0_{el} is the standard electrolyte potential, $c^0_{O_2,el}$ is the initial bulk concentration of O_2 in the electrolyte at OCV, and $c^0_{Li^+,el}$ is the initial bulk concentration of Li^+ in the electrolyte. The last term of Eq. 10 represents the effect of active species concentration on the cell performance. Any deviation of the concentrations from the standard concentration, viz, $c^0_{O_2,el}$ and $c^0_{Li^+,el}$, would reduce the cell (or half-cell) potential. Such a reduction in cell (or half-cell) potential that can be attributed to concentration of the active species, is defined by the last term of Eq. 10, and also termed as concentration overpotential.

The role of anode is limited to a line source of Li^+ at the anode/separator-cathode interface. The molar flux of Li^+ at the anode is obtained from a current density that is calculated from a Butler-Volmer equation based on the reduction reaction as,

$$Li^+_{el} + e^- \rightleftharpoons Li. \quad [11]$$

In the present work, we have formulated all the charge transfer reactions in reduction direction as commonly observed in electrochemistry literature. Also, in the Butler-Volmer kinetics that we have used, the current density expression is derived for a reduction reaction that adjusts the sign of current as positive or negative depending on the electrode overpotential during cell discharge i.e. positive for anode and negative for cathode. Consequently, the anode charge transfer reaction is modeled with the help of a modified Butler-Volmer equation that relates the anodic current density (i^A_{an}) to the activation overpotential as,

$$i^A_{an} = Fk^0_{an}\left(\frac{c_{Li^+,el}}{c^{ref}}\right)^{1-\alpha}\left\{e^{\alpha F\eta^{act}_{an}/(RT)} - e^{-(1-\alpha)F\eta^{act}_{an}/(RT)}\right\} \quad [12]$$

where, $k^0_{an} = 1 \times 10^{-3}$ mol/(m^2 · s) is the assumed rate of Li^+ reduction reaction (which is sufficiently fast not to contribute to overall cell overpotentials), $\alpha = 0.5$ is the symmetry factor, and η^{act}_{an} the anodic activation overpotential represented as,[48]

$$\eta^{act}_{an}(r) = \Delta\phi_{an}(r) - \Delta\phi^{eq}_{an}(r) \quad [13]$$

where, $\Delta\phi_{an}(r) = \phi_{an} - \phi_{el}(r)|_{z=0}$ is the local Galvani potential difference between the electrode (ϕ_{an}) and electrolyte (ϕ_{el}) at the separator/anode-cathode interface. It has to be noted that a low ohmic resistance of the electrode is assumed, hence the radial dependence of ϕ_{an} is ignored. $\Delta\phi^{eq}_{an}$ is the equilibrium Galvani potential as per the Nernst equation,

$$\Delta\phi^{eq}_{an}(r) = \Delta\phi^0_{an} + \frac{RT}{F}\ln\left(\frac{c_{Li^+,el}(r)}{c^0_{Li^+}}\right) = \phi^0_{an} - \phi^0_{el} + \frac{RT}{F}\ln\left(\frac{c_{Li^+,el}(r)}{c^0_{Li^+}}\right). \quad [14]$$

Again, the last term is the concentration overpotential (here at the anode).

We use the anode as electronic potential reference, that is, $\phi^0_{an} = \phi_{an} = 0$, and the unpolarized electrolyte as ionic potential reference, that is, $\phi^0_{el} = 0$. Using these references, the anode activation overpotential can be written as,

$$\eta^{act}_{an}(r) = \left[-\frac{RT}{F}\ln\left(\frac{c_{Li^+,el}(r)}{c^0_{Li^+}}\right) - \phi_{el}(r)\right]_{z=0}. \quad [15]$$

Consequently, the cell overpotential is given as,

$$\eta_{cell} = \phi_{ca} - \phi^0_{ca} \quad [16]$$

which is the closing equation, providing η_{cell} as independent variable.

Equations 9, 10, 15, 16 are a full representation of the (over)-potential distributions in the cell. The concentrations $c_{Li^+,el}(r, z)$ and $c_{O_2,el}(r, z)$ as well as the ionic potential $\phi_{el}(r, z)$ are provided by the transport model, as given in the next section.

Transport in porous cathode.—Two cathode models are presented in this study that represent two different configurations of porous cathode filled with electrolyte. The first configuration consists of the porous electrode completely flooded by the electrolyte (referred hereby as the flooded electrode model). In the second configuration, the electrolyte is assumed to wet completely the porous electrode surface but does not fill the pores (referred hereby as gas diffusion electrode (GDE) model). Figure 2 shows the schematics of the two approaches used. The respective model equations for both configurations are discussed in the sections below.

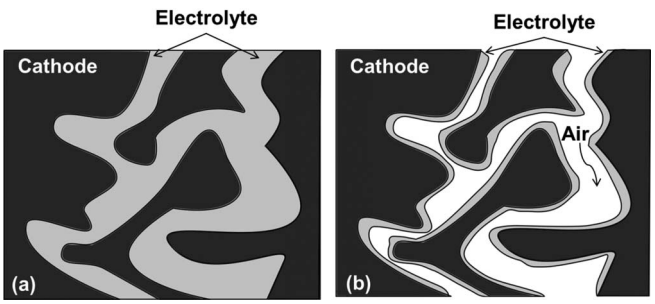

Figure 2. Schematics for the (a) flooded electrode model, (b) gas diffusion electrode (GDE) model.

Flooded cathode model.—In this cathode model, the electrolyte is considered as a static, continuous medium that completely fills the porous cathode. Consequently, our focus is limited to Li^+ and O_2 transport in the electrolyte. This model is based on the hypothesis that O_2 comes into contact with the electrolyte at the GDL-cathode interface and dissolves in the electrolyte depending on the partial pressure of oxygen in the GDL. Henry's law[50] is used to define the GDL-cathode interfacial concentration as,

$$c_{O_2,el} = H_{O_2} \cdot p_{O_2,GDL} \quad [17]$$

where, H_{O_2} is the Henry's constant. O_2 further diffuses through the electrolyte filled in the electrode pores to participate in the electrochemical reaction occurring at the electrode-electrolyte interface, the kinetics of which is given by the Butler-Volmer equation (Eq. 8). The resulting O_2 transport equation can be written as a partial differential equation in concentration of O_2 in the electrolyte ($c_{O_2,el}$),

$$\frac{\partial\left(\varepsilon_{ca} c_{O_2,el}\right)}{\partial t} - \nabla \cdot \left(D^{eff}_{O_2,el} \nabla c_{O_2,el}\right) = \dot{s}_{O_2,el} \quad [18]$$

where, $D^{eff}_{O_2,el} = \varepsilon_{ca}^{1.5} D_{O_2,el}$ is the effective diffusion coefficient of species in the electrolyte considering Bruggeman's correction and $\dot{s}_{O_2,el} = i^{\mathbb{V}}_{ca}/(nF)$ is the rate of consumption of O_2 due to the electrochemical reaction (cf. Eq. 7).

Further, the ionic species flux ($\boldsymbol{N}_{i,el}$) in the electrolyte is considered as a combination of two major fluxes, namely, diffusion ($\boldsymbol{j}^{D}_{i,el}$) and migration ($\boldsymbol{j}^{M}_{i}$),

$$\boldsymbol{N}_{i,el} = \boldsymbol{j}^{D}_{i,el} + \boldsymbol{j}^{M}_{i,el} = -D^{eff}_{i,el} \nabla c_{i,el} - z_i F u^{eff}_i c_{i,el} \nabla \phi_{el} \quad [19]$$

where, $D^{eff}_i = \varepsilon_{ca}^{1.5} D_i$ is the diffusion coefficient, z_i is the valence and u^{eff}_i is the mobility of i^{th} species that is calculated from the Nernst-Einstein relation as, $u^{eff}_i = D^{eff}_i/(RT)$. The ionic current density in the electrolyte depends on the sum of the flux of all charged species in the solvent and can be written as,

$$\boldsymbol{i}_{ionic} = F \sum_i z_i \boldsymbol{N}_{i,el} = -F \sum_i z_i D^{eff}_{i,el} \nabla c_{i,el} - F^2 \nabla \phi_{el} \sum_i z_i^2 u^{eff}_i c_{i,el}. \quad [20]$$

The lithium salt dissolved in the electrolyte is assumed to be a symmetric binary salt that dissociates completely in the solvent. The concentration of anion in the electrolyte is related to the concentration of Li^+ by assuming electro-neutrality ($\sum_i z_i c_{i,el} = 0$). Hence, it is sufficient to represent the species transport equation in the electrolyte as a PDE in concentration of Li^+ in the electrolyte ($c_{Li^+,el}$),

$$\frac{\partial\left(\varepsilon_{ca} c_{Li^+,el}\right)}{\partial t} - \nabla \cdot \boldsymbol{N}_{Li^+,el} = \dot{s}_{Li^+,el} \quad [21]$$

where, $\dot{s}_{Li^+,el} = i^{\mathbb{V}}_{ca}/F$ is the rate of consumption of Li^+ in the electrolyte. Finally, by applying conservation of charge in the electrolyte, the ionic current can be related to the total volumetric current density in the electrolyte as,

$$\nabla \cdot \boldsymbol{i}_{ionic} = i^{\mathbb{V}}_{ca}. \quad [22]$$

At the GDL-cathode interface a continuity of mass flux is applied,

$$\boldsymbol{n} \cdot \left(\rho_{air} \boldsymbol{u}_{air,GDL}\right) = \boldsymbol{n} \cdot \left(-D^{eff}_{O_2,el} \nabla c_{O_2,el}\right) M_{O_2} \quad [23]$$

where, $\boldsymbol{n}$ is the direction normal to the interface. At the same time, the species flux for H_2O and N_2 is taken to be 0 at the GDL-cathode interface for the gas phase transport (cf. Eq. 3).

At the cathode-separator/anode interface, the flux of Li^+ is given by the anodic current density as,

$$\boldsymbol{n} \cdot \boldsymbol{N}_{Li^+,el} = \frac{i^{A}_{an}}{F}. \quad [24]$$

The ionic current density at the cathode-separator/anode interface is given by,

$$\boldsymbol{n} \cdot \boldsymbol{i}_{ionic} = i^{A}_{an}. \quad [25]$$

The initial concentration of O_2 in the electrolyte is assumed to be $c_{O_2,in} = H_{O_2} \cdot p_{O_2,in}$. and that of Li^+ is assumed to be 1 M. The rest of the boundaries are considered to be impermeable ($n \cdot N_{i,el} = 0$) and insulated ($n \cdot i_{ionic} = 0$). The overall cell current density (in A/m^2 per button cell cathode surface area) is calculated as,

$$i_{cell} = \frac{\int i^{\mathbb{V}}_{ca} d\mathbb{V}}{\pi r^2_{ca}}. \quad [26]$$

Gas diffusion electrode model.—In the gas diffusion cathode model, the cathode pores are assumed to be covered by a thin layer electrolyte, cf. Figure 2b. The thickness of the electrolyte film (h_{el}) is calculated as,

$$h_{el} = \frac{\text{Volume fraction of the electrolyte}}{\text{Volume specific area}} = \frac{s_{el} \cdot \varepsilon_{ca}}{A^{\mathbb{V}}} \quad [27]$$

where, s_{el} is the volume fraction of electrolyte in the pore space, and ε_{ca} is the porosity of cathode. In the context of species transport, this case presents a much faster, convection dominated transport of O_2 into the pores of the cathode, where O_2 diffuses over the thin electrolyte film to participate in the ORR at the electrolyte-electrode interface. The gas flow in the porous cathode is modeled by mass conservation and air flow velocity is given by Darcy flow as,

$$\frac{\partial\left(\varepsilon_{air,ca} \rho_{air,ca}\right)}{\partial t} + \nabla \cdot \left(\rho_{air,ca} \boldsymbol{u}_{air,ca}\right) = \dot{s}_{O_2,ca} M_{O_2} \quad [28]$$

$$\boldsymbol{u}_{air,ca} = -\frac{\kappa_{air,ca}}{\mu_{air,ca}} \nabla p_{air,ca} \quad [29]$$

where, $\varepsilon_{air,ca} = (1 - s_{el})\varepsilon_{ca}$, $\rho_{air,ca} = p_{air,ca}/(RT)$ is the density of the gas phase, $p_{air,ca}$ is the pressure of the gas phase, $\kappa_{air,ca}$ is the permeability of the gas phase, and $\mu_{air,ca}$ is the viscosity of the gas phase. The gas-phase species transport is modeled by a convective-diffusive flow at the electrode as,

$$\frac{\partial\left(\varepsilon_{air,ca} c_{i,ca}\right)}{\partial t} - \nabla \cdot \left(D^{eff}_i \nabla c_{i,ca}\right) + \nabla \cdot \left(c_{i,ca} \boldsymbol{u}_{air,ca}\right) = \dot{s}_{i,ca} \quad [30]$$

where, $\dot{s}_{i,ca}$ is species consumption term in cathode volume in which $\dot{s}_{O_2,ca} = i^{\mathbb{V}}_{ca}/(nF)$ corresponds to the rate of charge transfer reaction and $\dot{s}_{H_2O,ca} = \dot{s}_{N_2,ca} = 0$. The diffusive transport of O_2 in the thin electrolyte film balances the rate of consumption of O_2 in the ORR, which is limited by the solubility of O_2 in the electrolyte corresponding to the local partial pressure of O_2 in the cathode. In order to satisfy this condition, an additional equation based on Fick's first law is solved balancing the O_2 consumption and O_2 dissolution,

$$\frac{i^{\mathbb{V}}_{ca}}{nF} = \frac{A^{\mathbb{V}} D_{O_2,el}\left(H_{O_2} p_{O_2,ca} - c_{O_2,el}\right)}{h_{el}} \quad [31]$$

where, $i^{\mathbb{V}}_{ca}$ is calculated by the modified Butler-Volmer equation (Eq. 8), $c_{O_2,el}$ is the concentration of O_2 at the electrode-electrolyte film interface. The electrolyte phase Li^+ transport is modeled by a Nernst-Planck based equation as shown in Eqs. 19–25.

Electrolyte properties.—In order to investigate electrolyte transport properties on the performance of the Li-air button cell, electrolytes from five major categories of solvents were considered, viz., aqueous (water),[51,52] ionic liquids (PYR14TFSI),[53–55] propylene carbonate (PC),[10,42,56,57] organosulfur (DMSO)[4,58,59], and protic ether (diglyme).[4] Although, there is a considerable lack of data for species transport properties for the mentioned solvents to their sensitivity on the solute compositions, salt concentrations, and cell operating conditions, this study is an effort to emphasize on the influence of physicochemical properties of solvents on cell performance that might be fine-tuned to achieve the required cell performance. Table II lists the transport properties of the electrolytes.

For diffusion-dominated transport in a flooded electrode, one of the performance-characterizing parameters is the mass transfer-limited

Table II. Transport properties of the electrolytes at 25°C considered in this work.

Solvent	Salt	Diffusivity/10^{-9} m^2/s		O_2 Solubility[a]/ $mol \cdot m^{-3}$	Density/ 10^3 $kg \cdot m^{-3}$	Viscosity/ $mPa \cdot s$	n
		O_2	Li^+				
Water[51,52]	LiOH	1.99	1.03	0.26	0.99	0.89	4
PYR14TFSI[53–55]	LiTFSI	1.20	0.01	2.89	1.43	60	2
PC[10,42,56,57]	$LiPF_6$	0.22	0.08	3.20	1.20	2.50	2
DMSO[4,58,59]	$LiPF_6$	1.67	2.66	2.09	1.10	1.99	2
Diglyme[4]	$LiPF_6$	4.40	0.12	6.50	0.94	1.88	2

[a]Solubility data is for 101.325 kPa of O_2 partial pressure.

current density, which can be expressed as,[60]

$$i_P = \frac{nFDc^0}{\delta} \quad [32]$$

where, n is the number of electrons transferred, F is the Faraday constant, D is the diffusivity of the active species in the electrolyte, c^0 is the bulk ionic concentration of the active species in solution, and $\delta \propto \sqrt{D/v}$ is the thickness of the Nernst diffusion layer.[61] When linear sweep voltammetry (LSV) is used as the characterization technique, the mass transport-limited peak current density i_P for O_2 as the active species is given by the Randles-Sevcik equation[61] as,

$$i_P = 2.68 \times 10^5 n^{3/2} \sqrt{v} c^0_{O_2} \sqrt{D_{O_2}} \quad [33]$$

where, $c^0_{O_2} = H_{O_2} \cdot p_{O_2}$ is the concentration of O_2 in the electrolyte from Henry's law. Hence, mass transport based limiting current density can be highly influenced by the supply of O_2 as the active species. Figure 3 shows the limiting current densities for various electrolytes as a function of voltage scan rate. It can be seen that diglyme has the best performance of all the electrolytes, as it has relatively the highest O_2 solubility and diffusivity.

However, the Randles-Sevcik equation is based on mass transport limitation in a 1D ideal planar electrode. On the contrast, in a realistic porous electrode, 2D/3D transport of gaseous and dissolved species is coupled to spatially non-uniform local current density and Li^+ transport. Hence, the results of the Randles-Sevcik equation can be only used as a qualitative estimate for comparison of electrolyte performance.

Simulation methodology.—The model equations presented above form a partial differential-algebraic equation system that allows calculating i_{cell} as function of applied cell overpotential η_{cell} while describing the species distribution in the cathode volume. The cell discharge is modeled by a linear sweep voltammetry (LSV) approach, where the cell overpotential η_{cell} is varied with time as,

$$\eta_{cell} = -v \cdot t \quad [34]$$

where, $v = \frac{dV}{dt} = 10^{-4}\ V/s$, is the voltage scan rate. Such a slow scan rate allows the cell to operate in the quasi-steady state, thus minimizing the contributions from non-faradaic currents like capacitive charging of the electrode at transient potential change,[61] justifying our approach of not considering such effects in the current work. The negative η_{cell} represents the overpotential during cell discharge. For the flooded electrode model, the simulations were performed until an overpotential of –0.5 V. It was observed that at large overpotentials (< –0.5 V), a high current density led to large source terms in the governing equations. Also, high concentration gradient of lithium ion at the anode-separator/cathode boundary was observed at high currents, which led to the necessity of using fine mesh at the boundary. These effects made the solver use finer time steps, leading to longer convergence times. Consequently, a compromise was made in this study to limit the simulation at –0.5V for the flooded electrode model. However, it will be observed in the following sections that within the scope of the present study, one can have the necessary information for comparing the electrolyte performance and electrode thickness of a Li-air cell under discharge conditions until an overpotential of –0.5 V.

The model was implemented and simulated in COMSOL Multiphysics[62] using the PARADISO direct solver with BDF based variable time stepping. The 2D geometry was meshed using rectangular elements with mesh refinement at the boundaries. A mesh convergence study was performed to optimize the solution accuracy and simulation time. The average time taken to perform one LSV simulation is around 20 minutes on a Windows PC with Intel Core i7 processor with 3.6 GHz CPU frequency and 32 GB RAM.

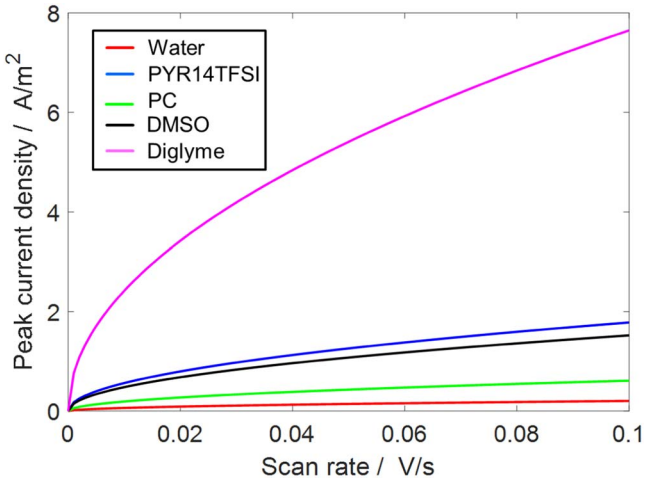

Figure 3. Theoretical estimates of limiting current density as a function of voltage scan rates as given by the Randles-Sevcik equation.

Results and Discussion

Characterization of the cell performance.—Figure 4 shows the effect of cell overpotential on current density for five different electrolytes for a flooded electrode. A comparison with an ideal Butler-Volmer current density (i_{BV}) is also provided that represents a cathode without any mass and charge transport losses ($\eta^{conc}_{ca} = 0$ and $\eta^{ohm}_{ca} = 0$). Such an ideal current density can be written as,

$$i_{BV} = Fk^0_{ca}\left(\frac{c^0_{O_2}}{c^{ref}}\right)^{(1-\alpha)/n}\left(\frac{c^0_{Li^+}}{c^{ref}}\right)^{1-\alpha} A^{\mathbb{V}} \times \left\{e^{\alpha F\eta^{act}_{ca}/(RT)} - e^{-(1-\alpha)F\eta^{act}_{ca}/(RT)}\right\}. \quad [35]$$

In this idealized case, the cathode activation overpotential varies as the applied cell overpotential ($\eta^{act}_{ca} = \eta_{cell}$). Li-air cells in which the electrolytes have low mass and charge transport losses have a low mass and charge transport overpotential. Theoretically, such cells would demonstrate a current density approaching the ideal i_{BV}. Figure 4 shows that species transport properties in the electrolytes

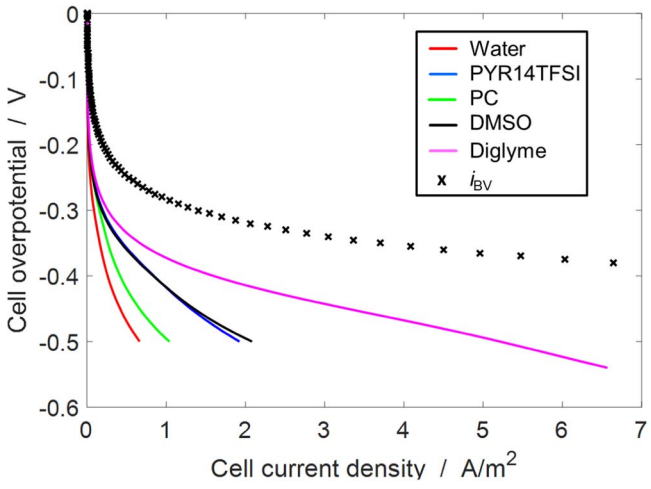

Figure 4. Comparison of cell performance for different electrolytes in a flooded cathode. Butler-Volmer current (i_{BV}) is provided as a reference value of an ideal electrode without any mass transport losses.

have a significant role in the cell performance. Diglyme, which has the highest O_2 solubility and diffusivity, shows the best performance. Water with lowest O_2 solubility has the poorest performance of the mentioned electrolytes despite the large Li^+ diffusivity. Our simulations are also consistent with the electrolyte performance predictions from Randles-Sevcik equation (cf. Figure 3). Further, PC has a better performance than water, where the former has lower O_2 diffusivity and higher solubility than the latter. This observation leads to the conclusion that electrolytes with high O_2 solubility should be preferred over high O_2 and Li^+ diffusivity, when other parameters are comparable. Also, as seen in Eq. 8, the local volumetric current density is a function of the local concentration of the active species in the electrolyte phase. Hence, solubility of active species is indeed a very important parameter for cell performance. However, to sustain a high local current density, the high rate of consumption of species must be complemented by an equally fast species transport, where the role of diffusivity becomes important. Henceforth, diglyme is chosen as the reference solvent for comparison of cell performance w.r.t. different cathode models and other parameters.

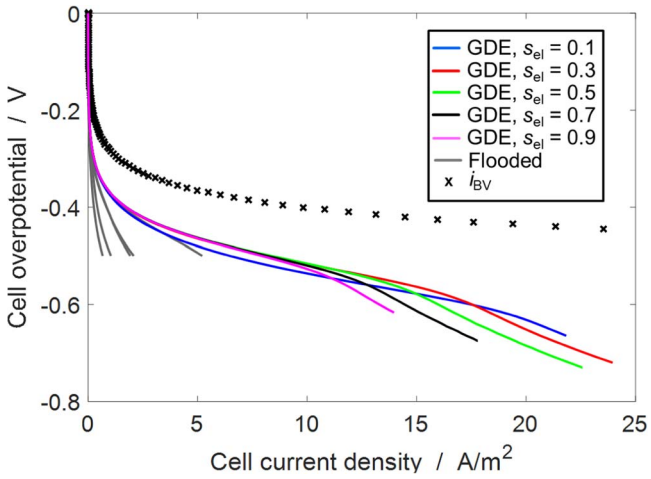

Figure 5. Cell performance for diglyme as electrolyte in a GDE configuration with five different saturations s_{el}. The gray curves show the data from flooded configuration in Figure 4 for comparison of scale. Butler-Volmer current (i_{BV}) is provided as a reference value of an ideal electrode without any mass transport losses.

Figure 5 shows the cell performance with diglyme as the solvent in flooded and GDE configurations with different electrolyte saturations s_{el}. It can be observed that the performance of cells in GDE (convection dominated transport) configuration is better than that in the flooded (diffusion dominated transport) configuration. The variation of cell performance with s_{el} can be associated with change in pore volume available for gas transport. A low s_{el} provides more volume for gas transport, enhancing O_2 supply. However, low s_{el} also leads to a reduced supply of Li ions in the electrolyte. This adversely affects the local volumetric current density (cf. Eq. 8). In the range of high current densities (10–20 A/m^2), one can see the cell performance reversal between the s_{el} of 0.1 and 0.9. Cell with s_{el} 0.9 performs better in low current density region where the supply of both Li^+ and O_2 are sufficient. However, in the high current density region, higher demand of O_2 leads to a better performance of cells with low s_{el}. Consequently, it can be seen that the optimal choice of electrolyte saturation has an important role in cell performance.

We also performed a "one parameter at a time" sensitivity analysis of the cell performance by observing the current density for various electrolyte transport parameters at overpotential of –0.5 V. The base configuration for the comparison was a 0.235 μm thick cathode flooded with diglyme. We assumed a measurement error of +10%/–5% in the parameters viz. diffusivity of Li^+ ($D_{Li^+,el}$), diffusivity of dissolved O_2 ($D_{O_2,el}$), and Henry's constant for O_2 (H_{O_2}). We observed that in the given range of measurement error, the variation in the current density for $D_{Li^+,el}$ is +0.14%/–0.08%, for $D_{O_2,el}$ is +2.93%/–1.59%, and for H_{O_2} is +3.81%/–2.04%. As a result, the sensitivity of the cell performance at the reference overpotential of –0.5 V is observed to be not so significant compared to an assumed measurement error range of the transport parameters. Further, the simulation results are observed to be more sensitive to O_2 transport parameters, especially O_2 solubility, than to Li^+ transport parameters.

2D distribution of active species.—In order to understand the spatial utilization of the cathode volume under cell operation, the spatial distribution of O_2 concentration and the local volumetric current density are investigated for different cathode models at an overpotential of –0.5 V. Figure 6 shows the O_2 concentration distribution in the flooded cathode and GDE at different electrolyte saturations. It is clearly observed that in the flooded cathode, there is a starvation of O_2 far from the GDL-cathode interface. This is because the diffusive transport is not fast enough to replenish the consumption of O_2 due to the ORR in cathode volume, away from the O_2 inlet. However, in the GDE a relatively fast replenishment of O_2 is expected due to convective air flow in the porous channels. Figures 6b–6d show that strong O_2 concentration gradients are observed along the cathode radius but not along the cathode thickness, irrespective of the electrolyte saturation. This observation can be explained by the fact that the thickness to radius aspect ratio of the cathode is quite high (ca. 1:100) and the air inlet hole is very small compared to the cathode radius. High concentration of O_2 along the cathode thickness just below the air inlet suggests that low aspect ratio or a larger inlet hole would lead to a more uniform O_2 distribution in the GDE. As observed, the role of inlet geometry for O_2 supply is an important aspect of the performance oriented cell design. Consequently, a future extension of the present study can also be performed toward optimizing the air inlet flow field by drawing parallels from polymer electrolyte membrane fuel cells flow field (PEMFC) design.[63] Further, due to the low pore volume available for air transport at high electrolyte saturations, stronger O_2 concentration gradients are observed in the radial direction at $s_{el} = 0.9$. Based on these observations, two design recommendations can be made: Firstly, a low cathode aspect ratio is recommended, and secondly, low electrolyte saturation should be used that improves the O_2 distribution in the cathode.

Since, there are two chemically active species in the cathode, distribution of O_2 does not give the complete idea of cathode volume utilization. The local volumetric current density determines the local rate of consumption of the active species and is a function of their concentrations (cf. Eq. 8). In a cell with ideal mass and charge

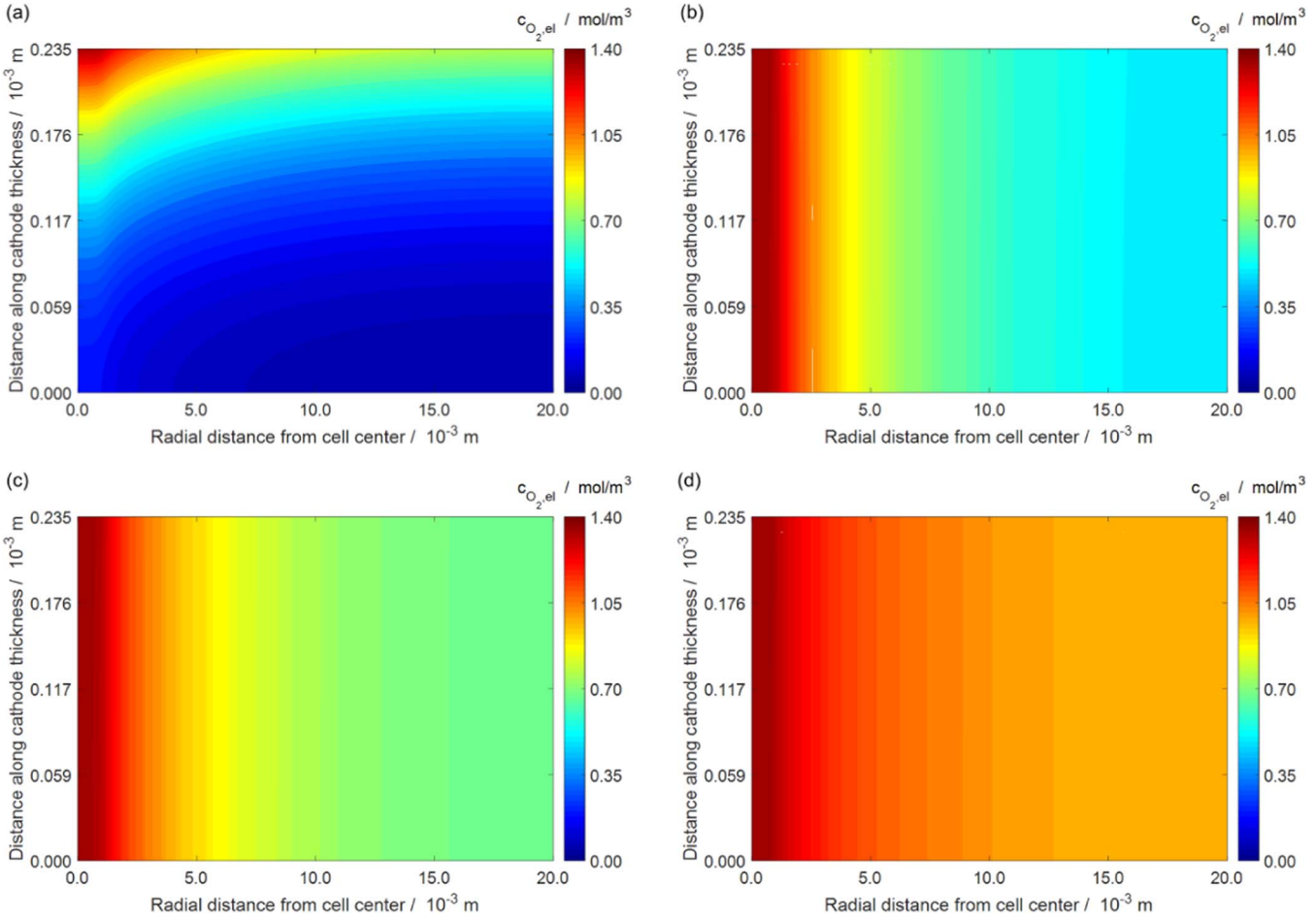

Figure 6. 2D distribution of O_2 concentration in diglyme at $\eta_{cell} = -0.5$ V, for (a) flooded electrode, (b) GDE with $s_{el} = 0.9$, (c) GDE with $s_{el} = 0.5$, and (d) GDE with $s_{el} = 0.1$.

transport, the volumetric current density is expected to be uniform throughout the cathode volume and equal to i_{BV}. Hence, a transport efficiency ($\eta_{transport}$) can be defined as the ratio of local volumetric current density to i_{BV} as,

$$\eta_{transport} = \frac{i_{ca}^{\mathbb{V}}}{i_{BV}}. \quad [36]$$

The transport efficiency describes the role of mass (O_2) and charge (Li^+) transfer losses on the distribution of volumetric current density in the cathode. The $\eta_{transport}$ is expected to be high in the electrode volume close to the reactant inlet, where the reactant concentration is equal to the maximum bulk concentration, while is low in electrode volume far away from the reactant inlet. Figure 7 shows the 2D distribution of $i_{ca}^{\mathbb{V}}$ and $\eta_{transport}$ in the cathode at overpotential of –0.5 V for flooded and GDE cathodes with different electrolyte saturations. It can be seen that in the flooded cathode, the maximum $i_{ca}^{\mathbb{V}}$ and $\eta_{transport}$ is observed close to the air inlet and becomes very low at the anode/separator-cathode interface (source of Li^+). Although, high O_2 diffusivity compared to Li^+ diffusivity would have suggested otherwise, a very low O_2 solubility as compared to Li^+ leads to faster consumption of O_2 than is supplied by diffusive flux toward the anode/separator-cathode interface. However, in GDE, the convective supply of O_2 throughout the cathode and its spontaneous solubility in the electrolyte makes the diffusion/migration transport of Li^+ performance limiting especially at low s_{el}. It has to be remembered that the effective diffusivity also reduces with reduction in electrolyte saturation as, $D_{i,el}^{eff} = (s_{el}\varepsilon_{ca})^{1.5} D_{i,el}$. At $s_{el} = 0.9$, high $i_{ca}^{\mathbb{V}}$ distribution is observed around the cell axis, $r = 0$, which is the location of air inlet hole too. Hence, in order to have a better $i_{ca}^{\mathbb{V}}$ distribution, a reduced aspect ratio or a bigger/additional inlet holes is recommended. At $s_{el} = 0.5$, a diagonally-symmetric $i_{ca}^{\mathbb{V}}$ is observed that suggests that the mass transfer losses are fairly balanced among the O_2 and Li^+. For very low electrolyte saturation such as $s_{el} = 0.1$, although the O_2 distribution is very good due to higher porous volume for air transport, Li^+ transport is severely reduced and is localized to the anode-cathode interface. This leads to the observed strongly non-uniform $i_{ca}^{\mathbb{V}}$ limited by Li^+ transport. Figure 8 shows the distribution of Li^+ concentration along the cathode thickness at the cell axis. Low electrolyte saturations lead to strong gradients in Li^+ concentration where its supply is diffusion limited to only the anode-cathode interface. This also explains the highly localized $i_{ca}^{\mathbb{V}}$ distribution near anode-cathode interface for low s_{el}.

In summary, the combined structural (saturation) and two-species transport properties can result in very different qualitative and quantitative distributions of reaction rate and electrode utilization. Vice versa, it can be seen that a desirable $i_{ca}^{\mathbb{V}}$ distribution and $\eta_{transport}$ of the cathode that can be achieved by appropriately choosing s_{el}.

Effect of electrolyte saturation and cathode thickness.—Choice of appropriate electrolyte saturation and cathode thickness helps to minimize the overall material content and consequently the cost of the cell. Having discussed the effect of electrolyte saturation on the local distribution of volumetric current density at an overpotential of –0.5 V, a global insight into the overall volume utilization of the cathode is needed at different current densities. At high current densities significant mass transport losses can be expected, creating highly localized $i_{ca}^{\mathbb{V}}$ near to reactant inlets. In order to quantify the

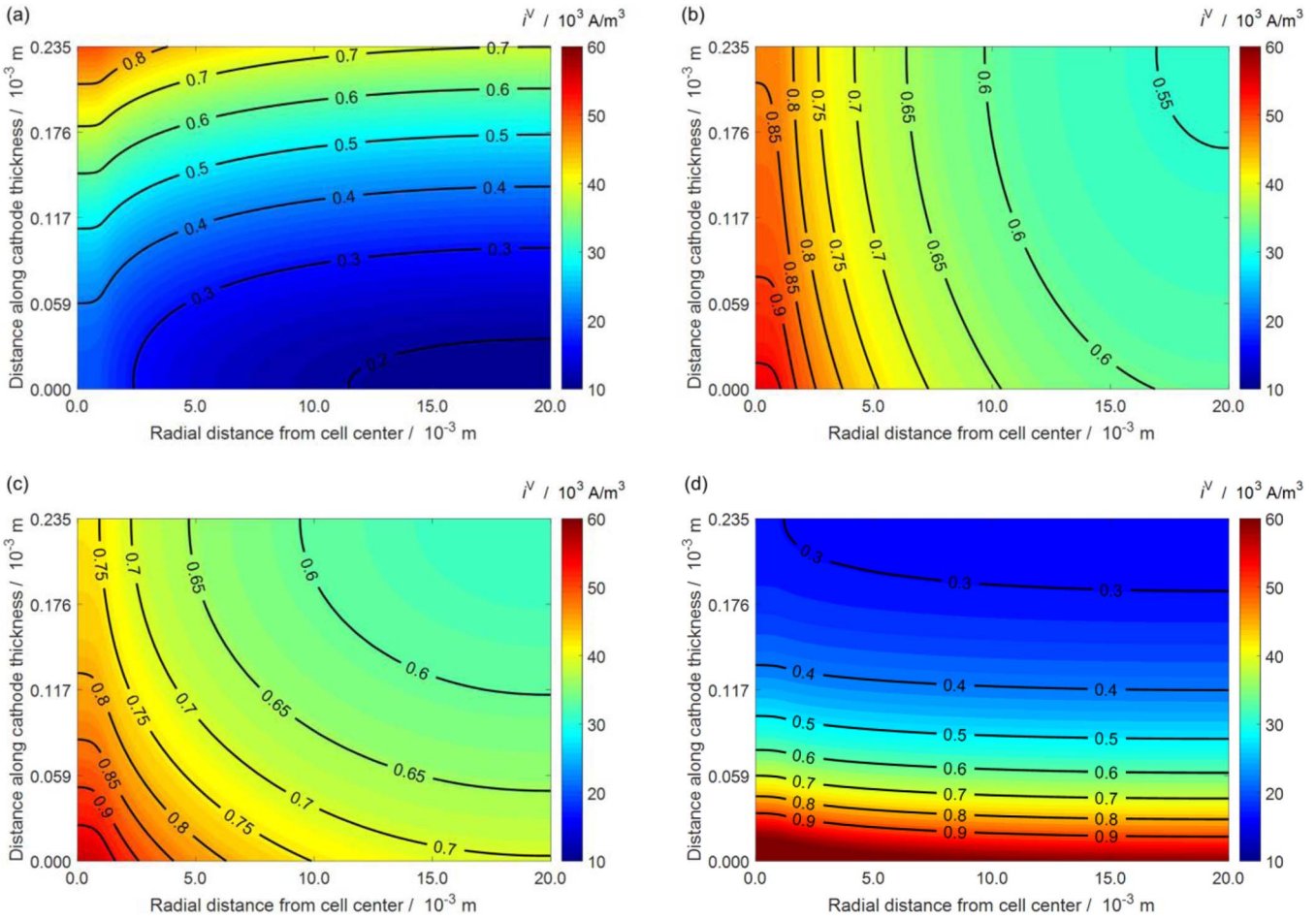

Figure 7. 2D distribution of volumetric current density for (a) flooded electrode, (b) GDE with $s_{el} = 0.9$, (c) GDE with $s_{el} = 0.5$, and (d) GDE with $s_{el} = 0.1$. The countour lines indicate the transport efficiency, $\eta_{transport}$.

effective volume utilization of the cathode, an "active cathode volume" parameter is introduced. Here, we define the active cathode volume $f_{active,90\%}$ as the percentage of cathode volume that produces 90% percent of the total current at a given overpotential. In order to obtain the active cathode volume, the 2D volumetric current density data are arranged as a 1D monotonically decreasing data, followed by numerical integration over the 1D index until the integral is 90% of the total integral over the entire length of 1D data. The active volume percent, $f_{active,90\%}$, is then the obtained volume as a percentage of the total cathode volume,

$$f_{active,90\%} = \frac{\mathbb{V}'}{\mathbb{V}_{total}} \times 100\% \quad [37]$$

where, V′ is the active volume producing 90% of the current produced in the entire cathode volume. It is calculated as,

$$\int_{\mathbb{V}'} i_{ca}^{\mathbb{V}} d\mathbb{V} = 0.9 \int_{\mathbb{V}_{total}} i_{ca}^{\mathbb{V}} d\mathbb{V}. \quad [38]$$

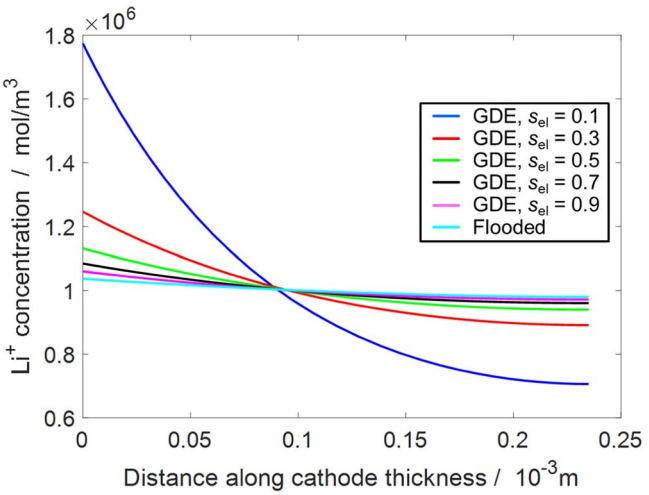

Figure 8. Variation of Li-ion concentration in diglyme at $\eta_{cell} = -0.5$ V along the cathode thickness at cell center ($r = 0$) for flooded and GDE cathodes with different electrolyte saturations s_{el}.

Figure 9 shows the variation in the active cathode volume for different cathode models as a function of cell current densities. Here, it can be seen that every cathode model (except GDE with $s_{el} = 0.1$) has a critical current density after which the active volume utilization falls strongly. The existence of such a critical current density suggests a strong mass transfer-limited supply and highly localized volumetric distribution of reactants. At low current densities (<1 A/m^2), $f_{active,90\%}$ converges to a value of 90%, which means a uniform volumetric distribution of current density. At higher currents, there is a sharp decrease in the active cathode volume and most of the current requirements of the cell are provided by a limited volume, which is typically a thin layer of the electrode. It has to be noted that in the GDE cathode the highest active volume is observed for an electrolyte saturation of $s_{el} = 0.3$. Due to the opposite effect of s_{el} on the mass transport of Li^+ and O_2, the lack of a monotonous trend for the active cathode volume for increasing or decreasing s_{el} can be explained.

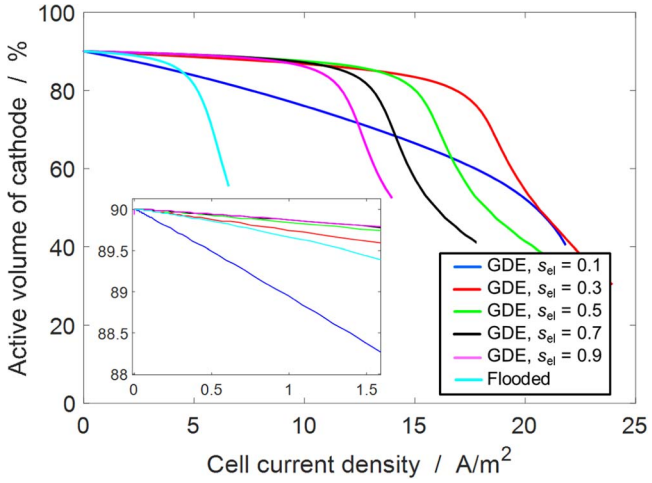

Figure 9. The active volume of cathode for diglyme at different cell current densities for flooded and GDE cathodes with different electrolyte saturations s_{el}.

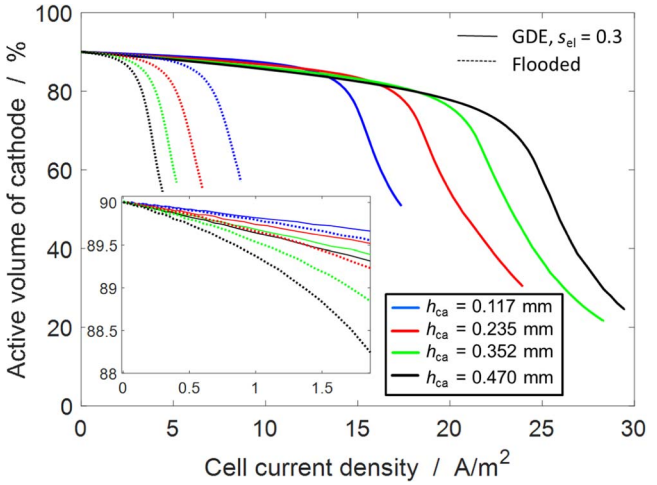

Figure 11. Comparison of active volume of cathode for diglyme at different cathode thickness in flooded cathode (dotted lines) and GDE with $s_{el} = 0.3$ (solid lines).

Figure 10 compares the cell current density at an overpotential of –0.5 V for different s_{el} and cathode thickness h_{ca}. The flooded electrode configuration is represented by $s_{el} = 1$. Thicker cathodes show better performance due to the availability of more electrode volume for current production. Overall, the cell performance decreases for very low and very high s_{el}. Also, variation in s_{el} has a stronger effect on cell performance for the thicker cathodes as the corresponding high current densities lead to more pronounced mass-transfer limitations.

Figure 11 shows the variation of active cathode volume as function of cell current density for flooded cathode and GDE with $s_{el} = 0.3$. In GDE, the active cathode volume and cell current density increases with cathode thickness, while in flooded cathode, they decrease upon increasing the cathode thickness. The reduction in active cathode volume in the flooded case at thick cathodes can be attributed to high mass transfer losses from species inlet to the overall cathode volume. At low cell current densities (<1 A/m^2), flooded cathode with $h_{ca} = 0.235$ mm has equivalent active volume as the GDE at $s_{el} = 0.3$ with its double cathode thickness, $h_{ca} = 0.470$ mm. This observation suggests an application oriented (low current densities) cell design can be highly optimized to use less material, thus reducing cell volume, mass, and cost.

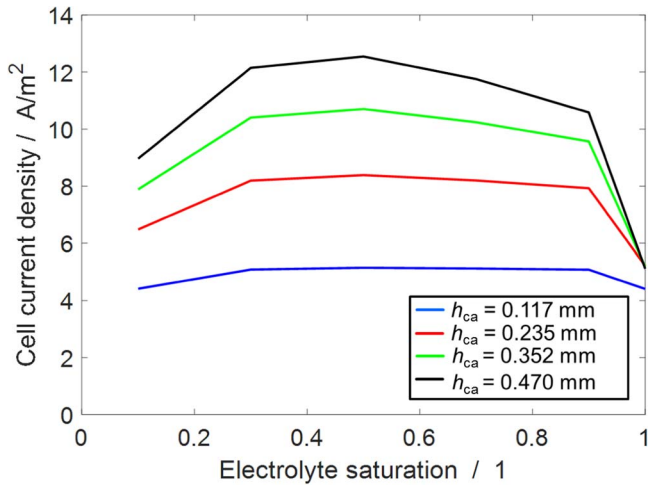

Figure 10. Cell performance comparison for different cathode thickness and electrolyte saturations for diglyme at $\eta_{cell} = -0.5$ V. The flooded cathode model is represented by $s_{el} = 1$.

It should be mentioned that a gas diffusion electrode, that is, a controlled partially wetted electrode, might be challenging to produce in reality. From the experimental work by Xia et al.,[34] creating a partially wetted electrode involves controlled evaporation of electrolyte in the porous cathode and depends on the wettability of the electrode surface by the electrolyte. The enhanced performance observed in a partially wetted as compared to the flooded electrode is qualitatively justified by this study. In an experiment performed by Xiao et al.,[37] increasing the electrolyte volume in the porous electrode made of Ketjen black, the cell performance increased. They attributed this to the volumetric expansion of the electrode due to electrolyte absorption that enhanced the porosity of the electrode, increasing the electrode-electrolyte interface for the ORR and thus increasing performance. However, they also did mention that such a significant volumetric expansion of electrode material was not observed for other carbon-based electrodes and was specific to Ketjen-black. Since, no volume expansion of either the electrolyte or the electrode is considered in the present model, such effects have not been observed.

Conclusions

With the help of a 2D axisymmetric model, the transport-limited performance of a Li-air button cell was investigated. Parametrically, the main focus of this study was on the transport properties (diffusivity and solubility) of active species (Li^+, O_2) in five different electrolytes, electrolyte saturation in the porous cathode, and cathode thickness. As result, diglyme shows the best performance with respect to achievable current density and active electrode volume.

With the help of two distinct cathode configurations, namely, flooded cathode and GDE, we were able to distinguish between the two dominating transport phenomena (diffusion and convection) in the cathode and identify their contributions to the local and global cell performance. GDE configuration is observed to be the better choice as it allows a faster and deeper penetration of O_2 in the cathode, enhancing the volumetric utilization of the cathode. Also, a lower aspect ratio of the cathode geometry is found to be better for O_2 distribution in the cathode volume. The combined structural, wetting (saturation) and two-species transport properties were shown to result in very different qualitative and quantitative distributions of reaction rates and electrode utilization.

For further analysis, two parameters for the efficacy of species transport were proposed, firstly, the transport efficiency that gives a local insight into the distribution of mass transfer losses across the cathode volume, and secondly, the active electrode volume that gives a global insight into the cathode volume utilization at different current

densities. A parametric study of cathode thickness and electrolyte saturation in the gas diffusion electrode demonstrates the ability of the model to support the optimization of cell performance and electrode utilization and allows proposing an application-guided cell design.

This work is a modeling study based on experimentally-determined electrolyte properties taken from literature. The validation of the simulation results with experimental data needs to be subject of future investigations.

Acknowledgments

The authors thank Martin Krebs (VARTA Microbattery GmbH, Ellwangen) for detailed discussions on the button cell design. The authors also gratefully acknowledge the Federal Ministry of Education and Research (BMBF) for funding this work. This work is part of the LiBaLu project in the framework of the "Vom Material zur Innovation" initiative (03XP0029A).

References

1. J. Lu and K. Amine, *Energies*, **6**(11), 6016 (2013).
2. S. Ma, Y. Zhang, Q. Cui, J. Zhao, and Z. Peng, *Chinese Phys. B*, **25**(1:018204), (2016).
3. V. S. Bryantsev, J. Uddin, V. Giordani, W. Walker, D. Addison, and G. V. Chase, *J. Electrochem. Soc.*, **160**(1), A160 (2012).
4. C. O. Laoire, S. Mukerjee, K. M. Abraham, E. J. Plichta, and M. A. Hendrickson, *J. Phys. Chem. C*, **114**(19), 9178 (2010).
5. B. D. McCloskey, D. S. Bethune, R. M. Shelby, G. Girishkumar, and A. C. Luntz, *J. Phys. Chem. Lett.*, **2**(10), 1161 (2011).
6. K. M. Abraham, *J. Electrochem. Soc.*, **162**(2), A3021 (2015).
7. C. M. Burke, V. Pande, A. Khetan, V. Viswanathan, and B. D. McCloskey, *Proceedings of the National Academy of Sciences of the United States of America*, **112**(30), 9293 (2015).
8. D. Chalasani and B. L. Lucht, *ECS Electrochemistry Letters*, **1**(2), A38 (2012).
9. S. A. Freunberger, Y. Chen, Z. Peng, J. M. Griffin, L. J. Hardwick, F. Bardé, P. Novák, and P. G. Bruce, *J. Am. Chem. Soc.*, **133**(20), 8040 (2011).
10. J. Read, K. Mutolo, M. Ervin, W. Behl, J. Wolfenstine, A. Driedger, and D. Foster, *J. Electrochem. Soc.*, **150**(10), A1351 (2003).
11. K. R. Ryan, L. Trahey, B. J. Ingram, and A. K. Burrell, *J. Phys. Chem. C*, **116**(37), 19724 (2012).
12. B. J. Bergner, M. R. Busche, R. Pinedo, B. B. Berkes, D. Schröder, and J. Janek, *ACS Appl. Mater. Interfaces*, **8**(12), 7756 (2016).
13. B. J. Bergner, C. Hofmann, A. Schürmann, D. Schröder, K. Peppler, P. R. Schreiner, and J. Janek, *Phys. Chem. Chem. Phys.*, **17**(47), 31769 (2015).
14. B. J. Bergner, A. Schürmann, K. Peppler, A. Garsuch, and J. Janek, *J. Am. Chem. Soc.*, **136**(42), 15054 (2014).
15. Y. Chen, S. A. Freunberger, Z. Peng, O. Fontaine, and P. G. Bruce, *Nature Chem*, **5**(6), 489 (2013).
16. M. J. Lacey, J. T. Frith, and J. R. Owen, *Electrochem. Commun.*, **26**, 74 (2013).
17. Z. Liang and Y.-C. Lu, *J. Am. Chem. Soc.*, **138**, 7574 (2016).
18. D. Sun, Y. Shen, W. Zhang, L. Yu, Z. Yi, W. Yin, D. Wang, Y. Huang, J. Wang, D. Wang, and J. B. Goodenough, *J. Am. Chem. Soc.*, **136**(25), 8941 (2014).
19. D. Grübl, B. Bergner, D. Schröder, J. Janek, and W. G. Bessler, *J. Phys. Chem. C*, **120**(43), 24623 (2016).
20. R. Younesi, N. Singh, S. Urbonaite, and K. Edström, in *216th ECS Meeting*, p. 121, ECS (2010).
21. Z.-L. Wang, D. Xu, J.-J. Xu, and X.-B. Zhang, *Chemical Society reviews*, **43**(22), 7746 (2014).
22. C. J. Bondue, P. Reinsberg, A. A. Abd-El-Latif, and H. Baltruschat, *Physical Chemistry Chemical Physics*, **17**(38), 25593 (2015).
23. M. Balaish, A. Kraytsberg, and Y. Ein-Eli, *ChemElectroChem*, **1**(1), 90 (2014).
24. J. Hojberg, K. B. Knudsen, J. Hjelm, and T. Vegge, *ECS Electrochemistry Letters*, **4**(7), A63 (2015).
25. S. V. Sazhin, K. L. Gering, M. K. Harrup, and H. W. Rollins, *J. Electrochem. Soc.*, **161**(3), A393 (2013).
26. P. Albertus, G. Girishkumar, B. McCloskey, R. S. Sánchez-Carrera, B. Kozinsky, J. Christensen, and A. C. Luntz, *J. Electrochem. Soc.*, **158**(3), A343 (2011).
27. B. Horstmann, T. Danner, and W. G. Bessler, *Energy Environ. Sci.*, **6**(4), 1299 (2013).
28. I. Bardenhagen, M. Fenske, D. Fenske, A. Wittstock, and M. Bäumer, *J. Power Sources*, **299**, 162 (2015).
29. I. Bardenhagen, O. Yezerska, M. Augustin, D. Fenske, A. Wittstock, and M. Bäumer, *J. Power Sources*, **278**, 255 (2015).
30. W. Xu, J. Xiao, J. Zhang, D. Wang, and J.-G. Zhang, *J. Electrochem. Soc.*, **156**(10), A773 (2009).
31. J. P. Zheng, P. Andrei, M. Hendrickson, and E. J. Plichta, *J. Electrochem. Soc.*, **158**(1), A43 (2011).
32. Y. Wang and S. C. Cho, *J. Electrochem. Soc.*, **162**(1), A114 (2014).
33. P. Tan, W. Shyy, L. An, Z. H. Wei, and T. S. Zhao, *Electrochem. Commun.*, **46**, 111 (2014).
34. C. Xia, C. L. Bender, B. Bergner, K. Peppler, and J. Janek, *Electrochem. Commun.*, **26**, 93 (2013).
35. R. E. Williford and J.-G. Zhang, *J. Power Sources*, **194**, 1164 (2009).
36. D. Geng, N. Ding, T. S. A. Hor, S. W. Chien, Z. Liu, D. Wuu, X. Sun, and Y. Zong, *Adv. Energy Mater.*, **6**(9), 1502164 (2016).
37. J. Xiao, D. Wang, W. Xu, D. Wang, R. E. Williford, J. Liu, and J.-G. Zhang, *J. Electrochem. Soc.*, **157**(4), A487 (2010).
38. J. Adams and M. Karulkar, *Journal of Power Sources*, **199**, 247 (2012).
39. A. A. Franco and K.-H. Xue, *ECS Journal of Solid State Science and Technology*, **2**(10), M3084 (2013).
40. V. Bevara and P. Andrei, *J. Electrochem. Soc.*, **161**(14), A2068 (2014).
41. C. P. Andersen, H. Hu, G. Qiu, V. Kalra, and Y. Sun, *J. Electrochem. Soc.*, **162**(7), A1135 (2015).
42. T. R. Jow, K. Xu, O. Borodin, and M. Ue, *Electrolytes for Lithium and Lithium-Ion Batteries*, New York, NY, Springer New York (2014).
43. J. P. Neidhardt, D. N. Fronczek, T. Jahnke, T. Danner, B. Horstmann, and W. G. Bessler, *J. Electrochem. Soc.*, **159**(9), A1528 (2012).
44. T. Danner, B. Horstmann, D. Wittmaier, N. Wagner, and W. G. Bessler, *J. Power Sources*, **264**, 320 (2014).
45. M. Lindstrom and B. Wetton, *Heat Mass Transfer*, **53**(1), 205 (2017).
46. D. R. Lide, Editor, *CRC Handbook of Chemistry and Physics*, Boca Raton, Florida, USA, CRC press (2006).
47. M. A. Rahman, X. Wang, and C. Wen, *J. Electrochem. Soc.*, **160**(10), A1759 (2013).
48. P. W. Atkins and J. D. Paula, *Atkins' Physical Chemistry*, Oxford, Great Britain, Oxford University Press (2006).
49. W. G. Bessler, S. Gewies, and M. Vogler, *Electrochim. Acta*, **53**, 1782 (2007).
50. W. Henry, *Philosophical Transactions of the Royal Society of London*, **93**(0), 29 (1803).
51. P. Han and D. M. Bartels, *J. Phys. Chem.*, **100**(13), 5597 (1996).
52. M. Laliberte, *Journal of Chemical & Engineering Data*, **52**(2), 321 (2007).
53. S. Monaco, A. M. Arangio, F. Soavi, M. Mastragostino, E. Paillard, and S. Passerini, *Electrochim. Acta*, **83**, 94 (2012).
54. H. Yoon, P. C. Howlett, A. S. Best, M. Forsyth, and D. R. MacFarlane, *J. Electrochem. Soc.*, **160**(10), A1629 (2013).
55. F. Castiglione, A. Famulari, G. Raos, S. V. Meille, A. Mele, G. B. Appetecchi, and S. Passerini, *The Journal of Physical Chemistry B*, **118**(47), 13679 (2014).
56. K. Hayamizu, *J. Chem. Eng. Data*, **57**(7), 2012 (2012).
57. T. Doi, R. Masuhara, M. Hashinokuchi, Y. Shimizu, and M. Inaba, *Electrochimica Acta*, **209**, 219 (2016).
58. S.-h. Jung, F. Federici Canova, and K. Akagi, *J Phys Chem A*, **120**(3), 364 (2016).
59. D. T. Sawyer, G. Chiericato, C. T. Angelis, E. J. Nanni, and T. Tsuchiya, *Anal. Chem.*, **54**(11), 1720 (1982).
60. C. G. Zoski, *Handbook of electrochemistry*, Amsterdam, Boston, Elsevier (2007).
61. A. J. Bard and L. R. Faulkner, *Electrochemical methods: Fundamentals and Applications*, New York, Wiley (2001).
62. *COMSOL® Multiphysics v. 5.2.*, Stockholm, Sweden, COMSOL AB.
63. X. Li and I. Sabir, *International Journal of Hydrogen Energy*, **30**(4), 359 (2005).